

Application of the three-component bidirectional reflectance distribution function model to Monte Carlo calculation of spectral effective emissivities of nonisothermal blackbody cavities

Alexander Prokhorov* and Nina I. Prokhorova

Virial International, LLC, 538 Palmspring Dr., Gaithersburg, Maryland 20878, USA

*Corresponding author: avpro@virial.com

Received 15 August 2012; revised 14 October 2012; accepted 19 October 2012;
posted 19 October 2012 (Doc. ID 174363); published 20 November 2012

We applied the bidirectional reflectance distribution function (BRDF) model consisting of diffuse, quasi-specular, and glossy components to the Monte Carlo modeling of spectral effective emissivities for nonisothermal cavities. A method for extension of a monochromatic three-component (3C) BRDF model to a continuous spectral range is proposed. The initial data for this method are the BRDFs measured in the plane of incidence at a single wavelength and several incidence angles and directional-hemispherical reflectance measured at one incidence angle within a finite spectral range. We proposed the Monte Carlo algorithm for calculation of spectral effective emissivities for nonisothermal cavities whose internal surface is described by the wavelength-dependent 3C BRDF model. The results obtained for a cylindrical nonisothermal cavity are discussed and compared with results obtained using the conventional specular-diffuse model. © 2012 Optical Society of America

OCIS codes: 120.5630, 120.5700, 230.6080, 290.1483.

1. Introduction

Blackbody cavities imitating the perfect blackbody are widely used as calibration sources in optical radiometry and radiation thermometry [1,2] since spectral characteristics of their radiation can be computed using Planck's law. The distinction between thermal radiation of the real-world cavities and that of a perfect blackbody is described by the effective emissivity, which is determined by the cavity geometry, optical properties of the cavity walls, viewing conditions (i.e., geometry of collecting the cavity radiation), and the temperature distribution over the radiating surface. The spectral local directional effective emissivity of a nonisothermal cavity is defined as

$$\varepsilon_e(\lambda, \xi, \omega, T_{\text{ref}}) = \frac{L_\lambda(\lambda, \xi, \omega)}{L_{\lambda, \text{bb}}(\lambda, T_{\text{ref}})}, \quad (1)$$

where λ is the wavelength, ξ and ω are the positional and directional vectors, respectively, and L_λ and $L_{\lambda, \text{bb}}$ are the spectral radiance (in $\text{W} \cdot \text{m}^{-3} \cdot \text{sr}^{-1}$) of the cavity and the perfect blackbody at a reference temperature T_{ref} .

Since the cavity is nonisothermal, the reference temperature T_{ref} has to be introduced and assigned to the perfect blackbody for uniqueness of the effective emissivity determination. T_{ref} itself has no specific physical meaning; its choice, in general, is arbitrary. Depending on the choice of T_{ref} , the spectral effective emissivity of a nonisothermal cavity can take any positive value. The spectral radiance and radiance temperature of a cavity do not change their values at any choice of T_{ref} . In practice, the

temperature measured by a contact temperature sensor is commonly used for T_{ref} to keep effective emissivities of the nonisothermal cavity comparable with those for the isothermal case. The denominator in Eq. (1) is calculated according to Planck's law:

$$L_{\lambda,\text{bb}}(\lambda, T_{\text{ref}}) = c_1 \left\{ \pi \cdot \lambda^5 \left[\exp\left(\frac{c_2}{\lambda \cdot T_{\text{ref}}}\right) - 1 \right] \right\}^{-1}, \quad (2)$$

where $c_1 = 3.74177153(17) \times 10^{-16} \text{ W}\cdot\text{m}^2$ and $c_2 = 1.4387770(13) \times 10^{-2} \text{ m}\cdot\text{K}$ are the first and second radiation constants, respectively [3].

Spectral effective emissivities corresponding to the specific viewing conditions can be obtained by integration of $\varepsilon_e(\lambda, \xi, \omega, T_{\text{ref}})$ over appropriate spatial and angular domains.

Equation (1) implies that the temperature of the environment is much lower than that of the cavity so one can neglect the contribution of the background radiation falling on the cavity aperture, partially reflected by the cavity, and increasing the emergent radiant flux. When the contribution of the background radiation is non-negligible, it can be taken into account by considering the background as a perfect blackbody at a temperature T_{bg} . If spectral effective emissivities $\varepsilon_e(\lambda, \xi, \omega)$ of an isothermal cavity and $\varepsilon_e(\lambda, \xi, \omega, T_{\text{ref}})$ of a nonisothermal cavity are known for zero background, correction for the background radiation can be done analytically:

$$\varepsilon_e(\lambda, \xi, \omega, T_{\text{ref}}, T_{\text{bg}}) = \varepsilon_e(\lambda, \xi, \omega, T_{\text{ref}}) + [1 - \varepsilon_e(\lambda, \xi, \omega)] \times \frac{\exp\left(\frac{c_2}{\lambda T_{\text{ref}}}\right) - 1}{\exp\left(\frac{c_2}{\lambda T_{\text{bg}}}\right) - 1}. \quad (3)$$

Hereinafter, we will suppose that the background radiation is absent.

Another important quantity is the radiance temperature T_S of a blackbody radiator. At this temperature, the spectral radiance of a perfect blackbody at a particular wavelength λ equals the spectral radiance emitted by the cavity radiator at the same wavelength. The radiance temperature of a cavity can be expressed as

$$T_S(\lambda, \xi, \omega, T_{\text{ref}}) = c_2 \left\{ \lambda \ln \left[1 + \frac{\exp\left(\frac{c_2}{\lambda T_{\text{ref}}}\right) - 1}{\varepsilon_e(\lambda, \xi, \omega, T_{\text{ref}})} \right] \right\}^{-1}. \quad (4)$$

Measurements of effective emissivities are extremely difficult and can be usually conducted under conditions that differ from actual operational conditions of the blackbody radiator [4]. Therefore, computational methods remain an indispensable tool for determining effective emissivities of cavity radiators at the stages of their design and metrological certification.

Numerous computational methods have been developed for calculating effective emissivities during

past decades (see, e.g., reviews [5,6]). The greatest difficulty in precise calculations of effective emissivities is the accounting for angular distributions of optical radiation emitted by and reflected from the internal surface of a cavity. At the same time, these distributions are often the crucial factors for the precision of the effective emissivity calculation.

2. Statement of the Problem

In the earlier works on calculation of the effective emissivities, the perfect diffuse (Lambertian) model of reflection has been employed. With the extensive use of digital computers, the Monte Carlo ray tracing (MCRT) method began to dominate in the effective emissivity calculations (see, e.g., [7–12]). Currently, the uniform specular–diffuse (USD) model of reflection is the most widespread in this area [8–11]. The USD model consists of the perfect diffuse (Lambertian) and the angle-independent perfect specular components. The USD model is more realistic than each of its parts taken separately but might be too crude an approximation for blackbodies intended for calibrations of the highest precision.

Angular distribution of reflected radiation is comprehensively described by the bidirectional reflectance distribution function (BRDF) [13], which depends on both incidence and viewing directions. In practice, the BRDF is measured for several incidence angles and for discrete set of viewing angles only. Hence, the parametric BRDF models fitted to the experimental data and capable to correctly predict BRDF values for all incidence and viewing directions are required to use in MCRT.

The three-component (3C) monochromatic BRDF model developed especially for MCRT applications and the algorithm for fitting the model parameters to the experimental data was proposed in [14]. This model was incorporated into the MCRT algorithm for calculating effective emissivities of isothermal cavities for the same wavelength at which the BRDF is measured. However, real-world cavity radiators are always nonisothermal. Besides, radiometric calibrations frequently have to be conducted for many wavelengths within certain spectral range.

The main objectives of this work are (i) to make the 3C BRDF model wavelength dependent, (ii) to incorporate the wavelength-dependent model into the MCRT algorithm for nonisothermal cavities, and (iii) to compare results obtained using the 3C and the USD models.

3. 3C BRDF Model for Monochromatic Radiation

In the spherical coordinate system, the BRDF [13] is defined as

$$\begin{aligned} f_r(\lambda, \theta_i, \phi_i, \theta_v, \phi_v) &= \frac{dL_{\lambda,v}(\lambda, \theta_i, \phi_i, \theta_v, \phi_v)}{dE_{\lambda,i}(\lambda, \theta_i, \phi_i)} \\ &= \frac{dL_{\lambda,v}(\lambda, \theta_i, \phi_i, \theta_v, \phi_v)}{dL_{\lambda,i}(\lambda, \theta_i, \phi_i)d\Omega_i} [\text{sr}^{-1}], \end{aligned} \quad (5)$$

where θ and ϕ are the polar and azimuthal angles, respectively, L_λ is the spectral radiance, E_λ is the spectral irradiance, Ω is the solid angle; subscripts “i” and “v” denote incidence and viewing directions, respectively. For brevity, we will omit the dependence on the wavelength throughout this section.

We will consider only isotropic surfaces, which are invariant with respect to rotation around its normal (i.e., f_r depends on $|\phi_i - \phi_v|$ instead of ϕ_i and ϕ_v) and the BRDFs measured for unpolarized radiation. In the case of polarimetric BRDF measurements, half the sum of the mutually perpendicular polarimetric BRDFs should be used (see, e.g., [15]). A physically plausible BRDF model must obey the reciprocity principle and the energy conservation law. The dependence of the directional-hemispherical reflectance (DHR) on the incidence angle is expressed as

$$\rho(\theta_i) = \int_0^{2\pi} d\phi \int_0^{\frac{\pi}{2}} f_r(\theta_i, \phi_i, \theta_v, \phi_v) \sin \theta_v \cos \theta_v d\theta_v. \quad (6)$$

The most accurate effective emissivity calculations must be based on the experimentally determined BRDF of the cavity internal surface. As mentioned above, all possible combinations of the incidence and viewing directions are required for MCRT while BRDF measurements are mostly incomplete (very often, they are conducted in the plane of incidence, at one wavelength, and for several incidence angles only). Therefore, the mathematical models (analytical expressions, as a rule) are necessary to fill the gaps in experimental data without violating such BRDF fundamental properties as reciprocity and energy conservation. Numerous BRDF models for a variety of materials reflecting optical radiation due to various kinds of scattering phenomena have been developed in computer graphics, remote sensing, and other areas (see, e.g., [16,17]), but not all of them are suitable for MCRT.

The 3C BRDF model [14] developed earlier for MCRT calculations of effective emissivities of isothermal blackbody cavities is expressed by the weighted sum of three components:

$$f_{r3C} = k_d f_{r,d} + k_{qs} f_{r,qs} + k_g f_{r,g}, \quad (7)$$

where $f_{r,d}$, $f_{r,qs}$, and $f_{r,g}$ are BRDFs of diffuse, quasi-specular, and glossy components, respectively; $0 \leq k_d$, k_{qs} , $k_g \leq 1$ and

$$k_d + k_{qs} + k_g = 1. \quad (8)$$

For the diffuse component with the *partial* (this qualifier is introduced *ad hoc* by the authors) diffuse reflectance R_d , the Lambertian BRDF is used:

$$f_{r,d} = R_d/\pi. \quad (9)$$

For the quasi-specular and glossy components, the BRDF model proposed in [18] was adopted:

$$f_{r,qs,g}(\theta_i, \theta_v, \phi) = \frac{R_{qs,g}(\theta_h)}{\pi \sigma_{qs,g}} \exp \left[- \left(\frac{\tan \theta_h}{\sigma_{qs,g}} \right)^2 \right] \times \frac{2[1 + \cos \theta_i \cos \theta_v - \sin \theta_i \sin \theta_v \cos \phi]}{(\cos \theta_i \cos \theta_v)^4}, \quad (10)$$

where σ_{qs} and σ_g are dimensionless parameters, which are determined the angular widths of quasi-specular and glossy lobes, respectively; θ_h is the angle between the normal to the surface and the bisector of the incidence and the viewing directions.

The slightly modified Schlick's approximation [19] of Fresnel's reflection law was used for angular dependences of $R_{qs}(\theta_i)$ and $R_g(\theta_i)$:

$$R_{qs,g}(\theta_i) = \begin{cases} R_{qs,g,0} + (1 - R_{qs,g,0})(1 - \cos \theta_i)^5 & \text{if } R_{qs,g,0} > 0 \\ 0 & \text{if } R_{qs,g,0} = 0 \end{cases} \quad (11)$$

where $R_{qs,0}$ and $R_{g,0}$ are the partial reflectances for the quasi-specular and glossy components, respectively.

Actually, the quasi-specular and the glossy components differ only in the ranges of values taken by parameters σ_{qs} and σ_g : $\sigma_{qs} \ll \sigma_g$, so the quasi-specular component has a narrow spike while the glossy component has more wider lobe. Figure 1 presents an example of plots in the spherical coordinate

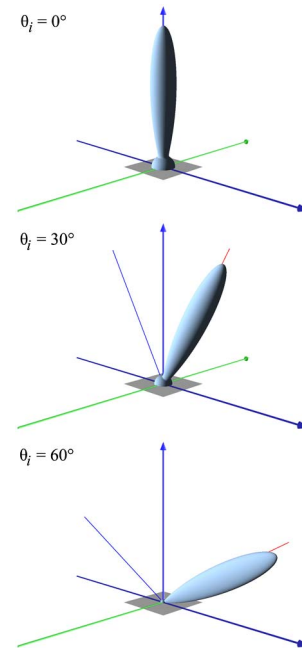


Fig. 1. (Color online) Plots of the 3C BRDF in spherical coordinates for three incidence angles θ_i ; $k_d = 0.7$, $k_{qs} = 0$, $k_g = 0.3$, $\sigma_g = 0.1$, $R_d = R_g(0^\circ) = 0.5$. All BRDFs are normalized by dividing by their maxima. The incident and specularly reflected rays are shown.

system for the 3C BRDF (very narrow quasi-specular spike is depicted as a specularly reflected ray).

Although the BRDF model Eq. (10) was initially proposed in [18] for random rough surfaces, it was found that it satisfactorily reproduces glossy lobes of different nature, for instance, those formed by volumetric scattering within layers of various paints and coatings.

The 3C BRDF model has eight parameters: k_d , R_d , k_{qs} , R_{qs} , σ_{qs} , k_g , R_g , and σ_g . Three of them are related through Eq. (8). In [14], the particle swarm optimization method [20] was used for fitting a 3C model to the BRDF values measured in the plane of incidence and, accordingly, to determine the model's parameters. When parameters are found, one can recover the three-dimensional BRDF, integrate numerically the expression for the 3C BRDF according to Eq. (6), and obtain the DHR value for any incidence angle. Because of linearity of integration in Eq. (6), the DHR ρ_{3C} equals

$$\rho_{3C}(\theta_i) = \rho_d + \rho_{qs}(\theta_i) + \rho_g(\theta_i), \quad (12)$$

where partial DHRs ρ_d , ρ_{qs} , and ρ_g are computed as

$$\rho_d = k_d R_d, \quad (13)$$

$$\begin{aligned} \rho_{qs,g}(\theta_i) &= k_{qs,g} \int_{\phi=0}^{2\pi} \int_{\theta_v=0}^{\pi/2} f_{r,qs,g}(R_{qs,g,0}(\lambda_0), \theta_i, \theta_v, \phi) \\ &\times \sin \theta_v \cos \theta_v d\theta_v d\phi. \end{aligned} \quad (14)$$

4. Wavelength-Dependent 3C BRDF Model

Our approach is based on the assumption that two kinds of measurement data are available: (i) the spectral DHR measured at one incidence angle $\theta_{i,0}$ for a wavelength range $[\lambda_{\min}, \lambda_{\max}]$ (the spectral DHR is usually measured using conventional devices such as integrating sphere accessory for spectral measuring equipment) and (ii) the BRDF measured in the plane of incidence at one wavelength $\lambda_0 \in [\lambda_{\min}, \lambda_{\max}]$ and for several incidence angles.

We assumed that parameters k_d , k_{qs} , k_g , σ_{qs} , and σ_g derived from the 3C model fitting in the plane of incidence at wavelength λ_0 as well as the relative contributions of the diffuse, quasi-specular, and glossy components of the DHR do not change their values throughout the wavelength range $[\lambda_{\min}, \lambda_{\max}]$; in other words, the shape of BRDF is supposed to be unchangeable within this spectral range. The spectral dependence of DHR is determined by spectral dependences of partial reflectances $R_d(\lambda)$, $R_{qs,0}(\lambda)$, and $R_{g,0}(\lambda)$, which, in turn, determine spectral dependences of partial DHRs ρ_d , ρ_{qs} , and ρ_g . Relative contributions of DHR components can be computed for the wavelength λ_0 and incidence angle $\theta_{i,0}$:

$$\begin{cases} \gamma_d = \rho_d(\lambda_0)/\rho^*(\theta_{i,0}, \lambda_0) \\ \gamma_{qs}(\theta_{i,0}) = \rho_{qs}(\theta_{i,0}, \lambda_0)/\rho^*(\theta_{i,0}, \lambda_0), \\ \gamma_g(\theta_{i,0}) = \rho_g(\theta_{i,0}, \lambda_0)/\rho^*(\theta_{i,0}, \lambda_0) \end{cases} \quad (15)$$

where the measured spectral DHR is asterisked; partial DHRs $\rho_d(\lambda_0)$, $\rho_{qs}(\theta_{i,0}, \lambda_0)$, and $\rho_g(\theta_{i,0}, \lambda_0)$ are computed using Eqs. (13) and (14) for the wavelength λ_0 .

Once partial DHRs $\rho_d(\lambda_0)$, $\rho_{qs}(\theta_{i,0}, \lambda_0)$, and $\rho_g(\theta_{i,0}, \lambda_0)$ are computed we can determine γ_d , $\gamma_{qs}(\theta_{i,0})$, and $\gamma_g(\theta_{i,0})$ according to Eq. (15). Since it was supposed that γ_d , $\gamma_{qs}(\theta_{i,0})$, and $\gamma_g(\theta_{i,0})$ do not depend on wavelength for all $\lambda \in [\lambda_{\min}, \lambda_{\max}]$, one can obtain three independent equations to find R_d , $R_{qs,0}$, and $R_{g,0}$:

$$\gamma_d \rho^*(\theta_{i,0}, \lambda) = k_d R_d(\lambda), \quad (16)$$

$$\begin{aligned} \gamma_{qs} \rho^*(\theta_{i,0}, \lambda) &= k_{qs} \int_{\phi=0}^{2\pi} \int_{\theta_v=0}^{\pi/2} f_{r,qs}(R_{qs,0}(\lambda_0), \theta_{i,0}, \theta_v, \phi) \\ &\times \sin \theta_v \cos \theta_v d\theta_v d\phi, \end{aligned} \quad (17)$$

$$\begin{aligned} \gamma_g \rho^*(\theta_{i,0}, \lambda) &= k_g \int_{\phi=0}^{2\pi} \int_{\theta_v=0}^{\pi/2} f_{r,g}(R_{g,0}(\lambda_0), \theta_{i,0}, \theta_v, \phi) \\ &\times \sin \theta_v \cos \theta_v d\theta_v d\phi. \end{aligned} \quad (18)$$

They have to be solved for each $\lambda \in [\lambda_{\min}, \lambda_{\max}]$. The solution of Eq. (16) is straightforward:

$$R_d(\lambda) = \gamma_d \rho^*(\theta_{i,0}, \lambda) / k_d. \quad (19)$$

Equations (17) and (18) are nonlinear equations for $R_{qs,0}$ and $R_{g,0}$, respectively. We used Brent's root-finding method [21] and two-dimensional adaptive quadratures [22] to compute integrals in Eqs. (17) and (18).

5. MCRT Algorithm for Spectral Effective Emissivities of Nonisothermal Cavities

The MCRT algorithm for computing the effective emissivity of an isothermal cavity whose internal surface can be described using the 3C BRDF model is based on Kirchhoff's law for the cavity effective emissivity and absorptance [14]. Because of thermodynamic equilibrium violation, Kirchhoff's law cannot be applied to nonisothermal cavities, but the Helmholtz reciprocity principle remains in force. This allows employing the backward ray tracing. The MCRT algorithm for nonisothermal cavities requires no changes compared with that for the isothermal case in parts related to generation of random directions for reflected rays, coordinate transformations, and finding the point of intersection of a ray with the cavity surface. A large number n of rays have to be launched into a cavity; their start points and directions are generated randomly, according to the viewing conditions, which have to be modeled. The statistical weight $w_{0k} = 1$ is assigned to the k th ray before tracing. Before each reflection, the type of reflection is chosen with the help of pseudorandom number u uniformly distributed from 0 to 1. If $u \leq k_d$, a random ray is generated according to the Lambertian BRDF; otherwise, if $u \leq k_d + k_{qs}$,

reflection is quasi-specular; otherwise it is glossy. After each reflection, the statistical weight is multiplied by the factor that is determined by the sampling procedure (see details in [14] and [18]):

$$w_{j,k} = w_{j-1,k} \times \begin{cases} R_d(\lambda) & \text{for diffuse reflection} \\ \frac{2R_{qs}(\lambda, \theta_{i,j-1,k})}{(1 + \cos \theta_{i,j-1,k} / \cos \theta_{v,j-1,k})} & \text{for quasi-specular reflection} \\ \frac{2R_g(\lambda, \theta_{i,j-1,k})}{(1 + \cos \theta_{i,j-1,k} / \cos \theta_{v,j-1,k})} & \text{for glossy reflection} \end{cases}, \quad (20)$$

where $\theta_{i,jk}$ and $\theta_{v,jk}$ are the incidence and viewing (reflection) angles, respectively; the index “ j ” denotes the number of reflection.

The ray is traced until it escapes the cavity; the backward ray tracing considers the last reflection point as the emission point of the ray propagated in the opposite direction, i.e., toward the observer. At the j th reflection point, the spectral radiance of the backward propagated k th ray comprises the radiation emitted and reflected at this point and is expressed by the following recurrence relation:

$$L_{\lambda,j,k}(\lambda) = (1 - w_{j+1,k})L_{\lambda,bb}(\lambda, T_{j+1,k}) + w_{j+1,k}L_{\lambda,j+1,k}, \quad (21)$$

where $L_{\lambda,bb}$ is the spectral radiance of the perfect blackbody expressed by Planck’s law, $T_{j+1,k}$ is the temperature of a cavity surface at the point of the $j + 1$ th reflection of the k th ray.

The spectral radiance of the k th backward propagated ray leaving the cavity can be written as

$$L_{\lambda,k}(\lambda) = [1 - w_{1,k}(\lambda)]L_{\lambda,bb}(\lambda, T_{1,k}) + \sum_{j=2}^{m_k} [1 - w_{j,k}(\lambda)]L_{\lambda,bb}(\lambda, T_{j,k}) \prod_{l=1}^{j-1} w_{l,k}(\lambda), \quad (22)$$

where m_k is the number of reflections in the k th ray trajectory. Finally, the estimator for the spectral directional effective emissivity of a cavity at a wavelength λ is

$$\varepsilon_e(\lambda, T_{\text{ref}}) = \frac{1}{nL_{\lambda,bb}(\lambda, T_{\text{ref}})} \sum_{k=1}^n L_{\lambda,k}(\lambda). \quad (23)$$

6. Numerical Example

To demonstrate the practical implementation of the algorithm and investigate its potential, we present numerical results obtained for normal and conical viewing conditions of a nonisothermal cavity formed by a conical bottom, a cylindrical middle part, and a flat diaphragm as it is depicted in Fig. 2. The following geometrical parameter of the cavity was used for all numerical experiments: conical bottom vertex angle $\beta = 60^\circ$, the cylindrical part radius $r_c = 1$,

the aperture radius $r_a = 0.75$, and the cavity length $z_2 = 6$.

Normal viewing conditions correspond to the case of the radiometer’s optical system focused at infinity;

the radius r_b of the viewing beam can be defined by an external diaphragm. These viewing conditions are modeled by generating rays that are parallel to the cavity axis and uniformly distributed over the circular cross section of the viewing beam. Conical viewing conditions reproduce the pinhole model mimicking the optical system that collects the cavity radiation onto the detector and are defined by the angular field of view (FOV) $\psi = 10^\circ$ and the axial coordinate z_f of the focal point. Such viewing conditions are modeled by generating random rays originated in the vertex of a ray cone and uniformly distributed within the conical solid angle with the apex angle ψ . The ray cone vertex can take a position $z_{f,\text{min}} \leq z_f \leq z_{f,\text{max}}$, where $z_{f,\text{min}}$ and $z_{f,\text{max}}$ are determined by the values of r_a and ψ (in our case, $z_{f,\text{min}} \approx -2.57$, $z_{f,\text{max}} \approx 14.57$). If $z_f < 0$, the focal point (ray cone vertex) is behind the cavity bottom.

Three simple (axisymmetric piecewise-linear, see Fig. 2) but realistic temperature distributions were

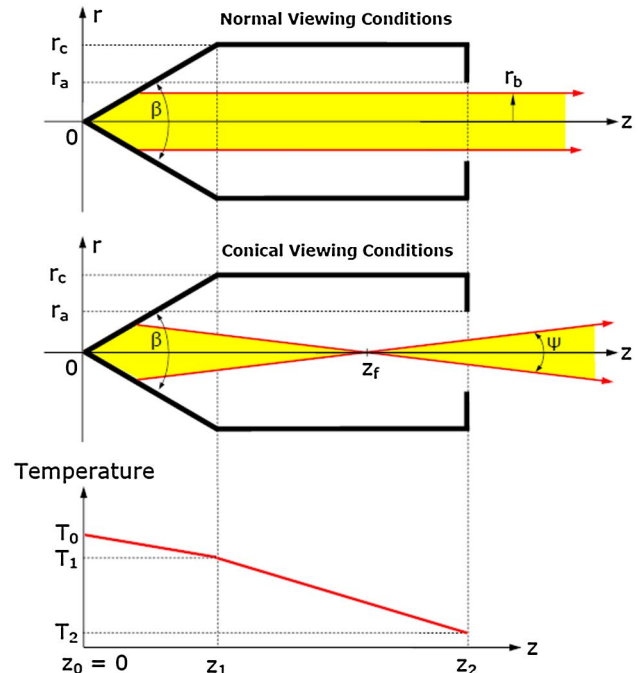


Fig. 2. (Color online) Schematics of cavity section, viewing conditions, and axial temperature distributions used for numerical experiments.

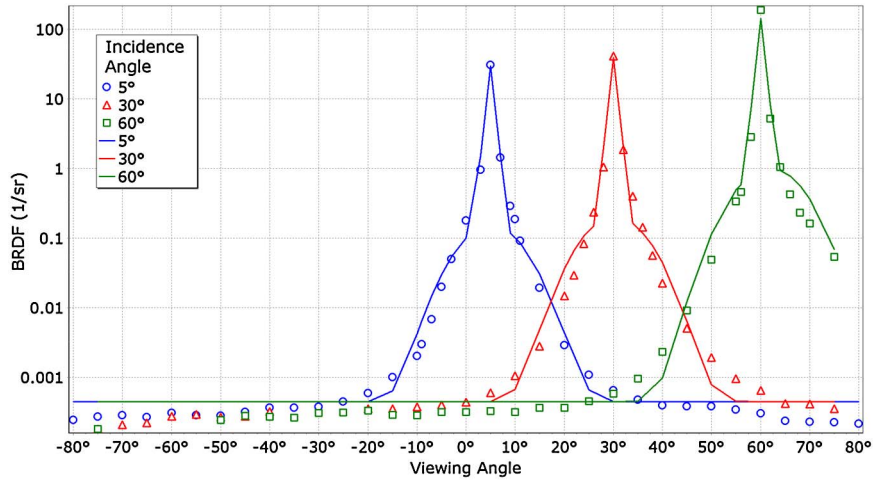


Fig. 3. (Color online) 3C BRDF model (lines) fitted to Z302 black paint BRDFs measured at 10.6 μm (symbols).

used for calculations. For all distributions, the reference temperature T_{ref} is equal to the temperature of the bottom vertex $T_0 = 350$ K; the temperature of the diaphragm is uniform and equal to the temperature of the cylindrical part edge $T_2 = 345$ K; $T_{\text{bg}} = 0$ K. The temperature T_1 at the interface of the conical bottom and cylindrical part is equal to 349.5, 349, and 348 K for the first, the second, and the third temperature distribution, respectively.

We supposed that all internal surface of a cavity is coated with the almost specular black paint Z302 widely used until now in low-temperature blackbodies and thermal detectors of optical radiation [23]. Its in-plane BRDF was measured at wavelength of 10.6 μm [24]. Figure 3 presents logarithmic plots of the measured in-plane BRDF and the fitted 3C model. The spectral DHR of Z302 was measured from near to far IR [25] at the incidence angle $\theta_{i,0} = 8^\circ$ using the Fourier-transform IR spectrometer and the integrating sphere coated with diffuse gold [26,27]; however, we used only the wavelength range from 8 to 12 μm near the maximum of the Planck distribution at 350 K. Within this spectral range, our assumption that parameters $k_d, k_{\text{qs}}, k_g, \sigma_{\text{qs}}$, and σ_g are wavelength independent seems plausible. Figure 4 shows the spectral DHR $\rho(\lambda, \theta_{i,0})$ (measured, smoothed, and sampled points) and its computed partial spectral DHRs $\rho_d(\lambda, \theta_{i,0})$, $\rho_{\text{qs}}(\lambda, \theta_{i,0})$, and $\rho_g(\lambda, \theta_{i,0})$.

We traced 10^6 rays for calculation of each spectral effective emissivity value. Repeated calculations show that the root mean square of the stochastic error in the spectral effective emissivity does not exceed $2 \cdot 10^{-4}$ and is less than $1 \cdot 10^{-4}$ in most cases. We have chosen the cavity black enough to neglect the background radiation. For the cavity with the uniform temperature of 350 K, the change of the spectral radiance at 10.6 μm introduced by the background radiation at 300 K is less 0.03%. This value is comparable with the uncertainty of calculations; therefore, the results obtained for $T_{\text{bg}} = 0$ K are applicable to all reasonable values of the background temperature.

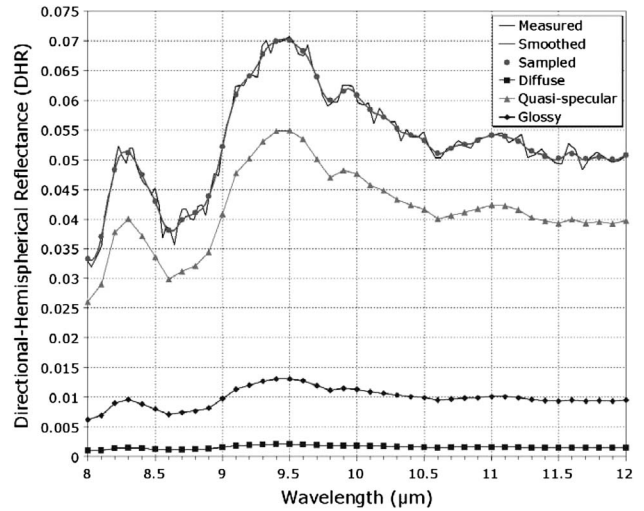


Fig. 4. Spectral DHR (measured, smoothed, and sampled from the smoothed curve) and partial spectral DHRs for diffuse, quasi-specular, and glossy components. Sampled values were used for numerical experiments.

A. Normal Viewing Conditions

Spectral effective emissivities computed for the viewing beam radii $r_b = 0.25$ and $r_b = 0.75$ are presented in Fig. 5. The effective emissivity for the isothermal case is greater than 0.9995. A decrease of the cavity walls temperature toward the aperture leads to decrease of the effective emissivities of nonisothermal cavity in comparison with isothermal one; the more, the greater temperature gradient along the cavity bottom. The lower values of the effective emissivities for $r_b = 0.75$ in comparison with those for $r_b = 0.25$ show that the temperature nonuniformity of the directly viewable area of a cavity has the greatest impact on the effective emissivity and thus confirms the analogous conclusion made earlier for the USD model of reflection [9]. Our finding agrees with the well-known fact that the minimization of the viewable area softens the requirements for the temperature uniformity of the radiating surface. Therefore, at the design of cavity radiators, the most attention

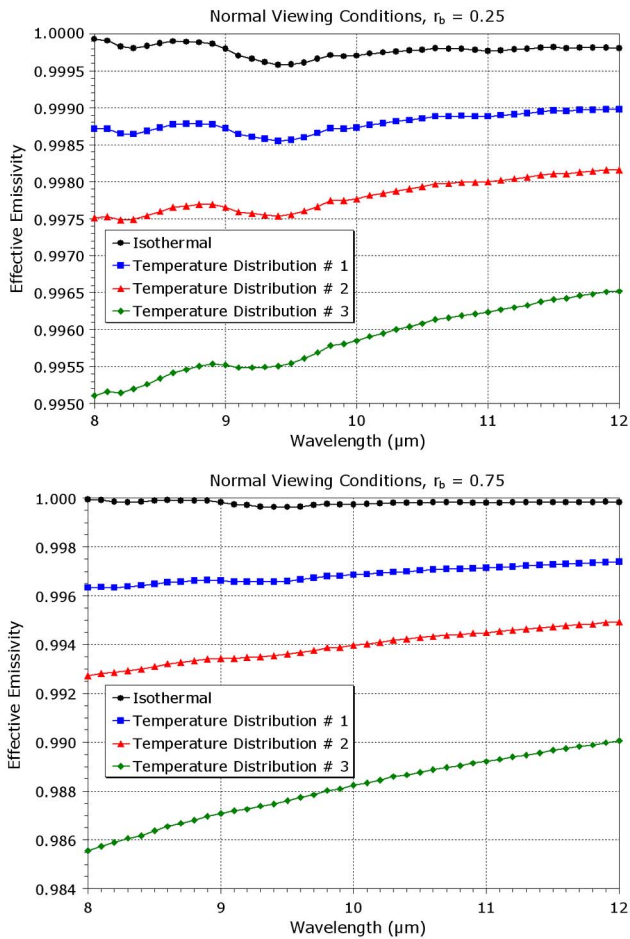


Fig. 5. (Color online) Spectral effective emissivities at normal viewing conditions for $r_b = 0.25$ (upper graph) and $r_b = 0.75$ (lower graph) computed for isothermal cavity and for three temperature distributions.

should be paid to ensuring temperature uniformity of viewable areas of a cavity surface; efforts to provide temperature uniformity of the entire cavity may be excessive.

Figure 6 shows dependences of the cavity radiance temperatures at $\lambda = 10.6 \mu\text{m}$ on the viewing beam radius r_b for three temperature distributions. These dependences are almost linear, which is explained by the linear and small temperature variation across the cavity bottom: the spectral radiance depends on temperature almost linearly within the range from 348 to 350 K.

B. Conical Viewing Conditions

Figures 7 and 8 show spectral effective emissivities computed for conical viewing conditions at four positions z_f of the focal point (the vertex of the conical viewing beam). It should be noted that, in distinction from the normal viewing conditions, the rays hit the cylindrical part of the cavity if z_f greater than approximately 13.

Spectral emissivity patterns obtained for $x_f = -2.5$ and $x_f = 2.5$ are similar though not identical because (i) the cavity bottom is observed at different angles

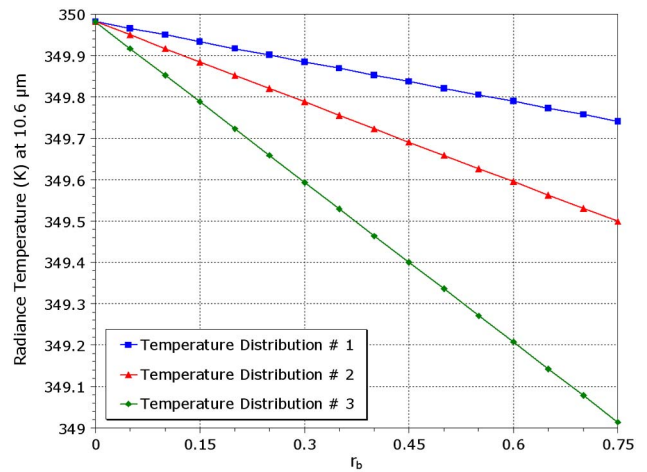


Fig. 6. (Color online) Dependences of the radiance temperatures at $10.6 \mu\text{m}$ on the viewing beam radius r_b of normal viewing conditions computed for three temperature distributions.

and (ii) viewable areas are slightly different for these two cases.

Despite the complexity of elaborating universal guidelines for the focal point optimal arrangement (behind or in front of the cavity bottom), we can deduce the following simple rule: the first (in terms of backward ray tracing) incidence angle should be minimal (since the reflectance increases for most materials with increasing the incidence angle), but the specularly reflected ray should not escape a cavity after the first reflection.

Figures 7 and 8 show that the influence of temperature nonuniformity is stronger in the shortwave spectral range. This is also consistent with the findings obtained earlier [9] for the USD model of reflection.

Figure 9 presents dependences of radiance temperatures at $10.6 \mu\text{m}$ computed for three temperature distributions on the focal point position z_f . As for normal viewing conditions, these dependences are almost linear while only the cavity bottom is directly viewable. For z_f greater than approximately 13, the rays begin to fall onto the cylindrical part at grazing angles. Because of increase of reflectance at large incidence angle and the discontinuous change of the axial temperature gradient, all radiance temperature curves undergo a dip for $z_f > 13$.

C. Comparison with the USD Reflection Model

In order to explore how large the difference is between results obtained with the 3C BRDF model and those obtained with the USD model of reflection, radiance temperature dependences presented in Figs. 6 and 9 were recomputed for the USD model with the same spectral DHR $\rho(\lambda)$. Since one-to-one correspondence between eight parameters of the 3C model and the diffusivity $D = \rho_d(\lambda)/\rho(\lambda)$ of the USD model is impossible, we adjusted the diffusivity value so that $\rho \cdot D$ for the USD model equals ρ_d for the 3C model at $\lambda = 10.6 \mu\text{m}$. The obtained value $D = 0.03$ was used for calculations. Figures 10 and 11 show

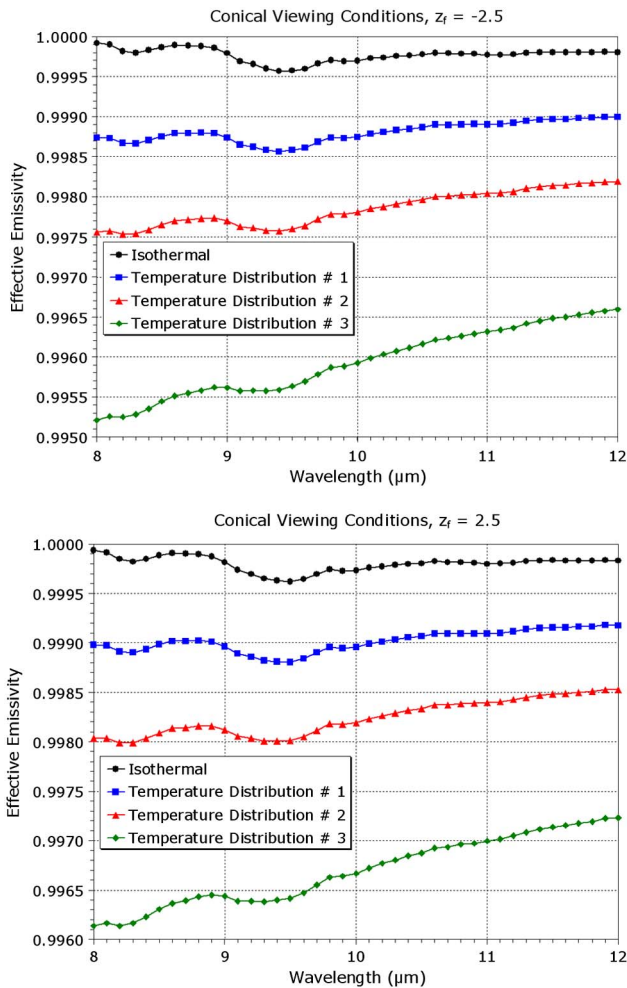


Fig. 7. (Color online) Spectral effective emissivities at conical viewing conditions for $z_f = -2.5$ (upper graph) and $z_f = 2.5$ (lower graph) computed for isothermal cavity and for three temperature distributions.

deviations of radiance temperatures at $10.6 \mu\text{m}$ computed using the USD reflection model from those computed using 3C BRDF model against parameters r_b and z_f of the normal and conical viewing conditions, respectively.

It was found that, for the normal viewing conditions, the difference between radiance temperatures computed using two models grows with the r_b increase but does not exceed 5 mK. This growth can be attributed to the finite width of the quasi-specular and the glossy lobes of the 3C model. As was shown for an isothermal cavity in [14], the finite width of the reflected beam in the 3C model leads to additional reflection from the cavity diaphragm, while the infinitely thin specularly reflected ray in the USD model always undergoes four successive reflections before escaping the cavity.

For the case of the conical viewing conditions, the difference is also relatively small while the viewing beam spans the cavity bottom only. As soon as rays begin to fall onto the cylindrical part, the difference between radiance temperatures computed using the 3C and the USD models increases sharply. This effect

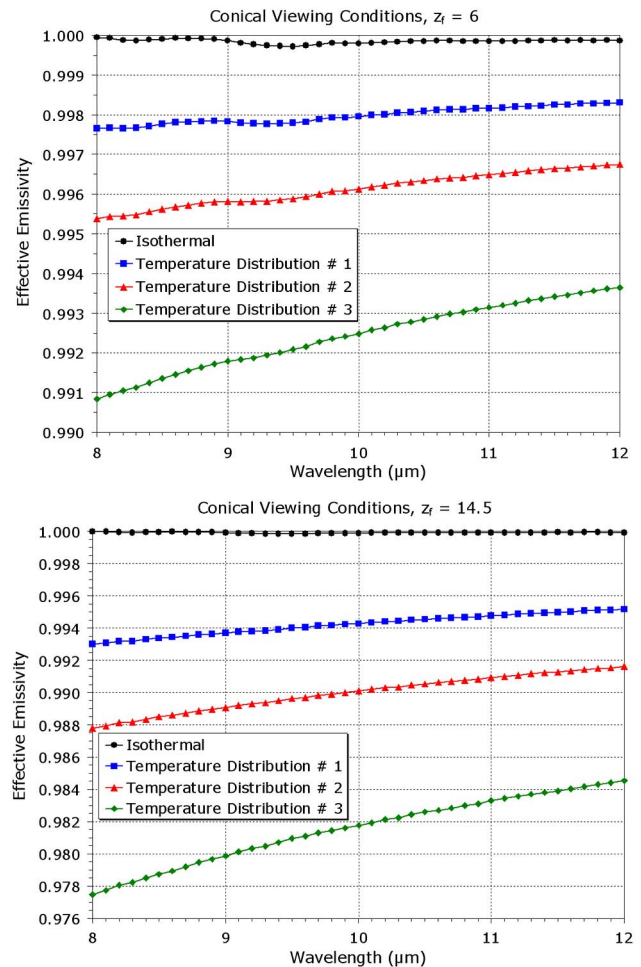


Fig. 8. (Color online) Spectral effective emissivities at conical viewing conditions for $z_f = 6$ (upper graph) and $z_f = 14.5$ (lower graph) computed for isothermal cavity and for three temperature distributions.

is due to the angular dependence of the quasi-specular and the glossy components of the 3C BRDF model on the incidence angle: rays fall onto the

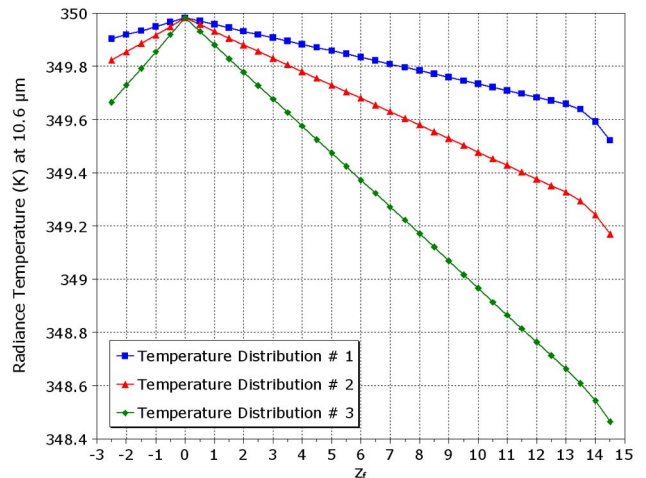


Fig. 9. (Color online) Dependences of radiance temperatures on the focal point position z_f of conical viewing conditions computed for three temperature distributions.

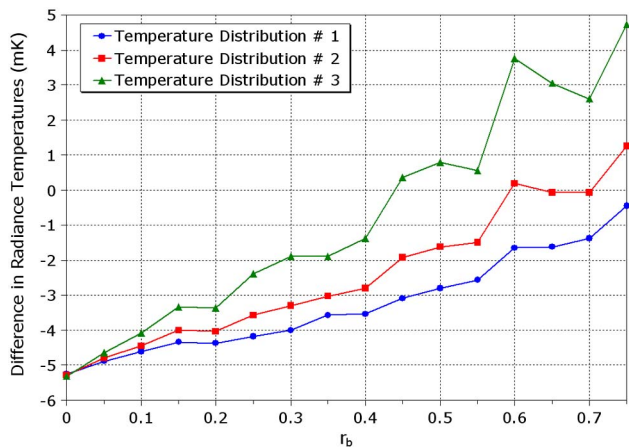


Fig. 10. (Color online) Deviation of radiance temperatures at $10.6 \mu\text{m}$ computed using the USD reflection model from those computed using 3C BRDF model. Difference in radiance temperatures is plotted as a function of the viewing beam radius r_b of normal viewing conditions.

cylindrical part of the cavity at grazing angles for which partial DHRs of these components increase rapidly (and the emissivity decreases correspondingly), while the reflectance of the USD model is angle-independent.

Blurry stepwise changes of curves in Figs. 10 and 11 occur because all specularly reflected radiation for the USD model is concentrated within the infinitely thin specular component. The effective emissivity and the radiance temperature dependences on the viewing conditions parameter are determined to a great extent by changing the number of reflections for each specularly reflected ray until it escapes the cavity. Distribution on incidence angles for rays within a conical FOV as well as presence of a small but nonzero diffuse component “blur” stepwise changes of the effective emissivity and the radiance temperature.

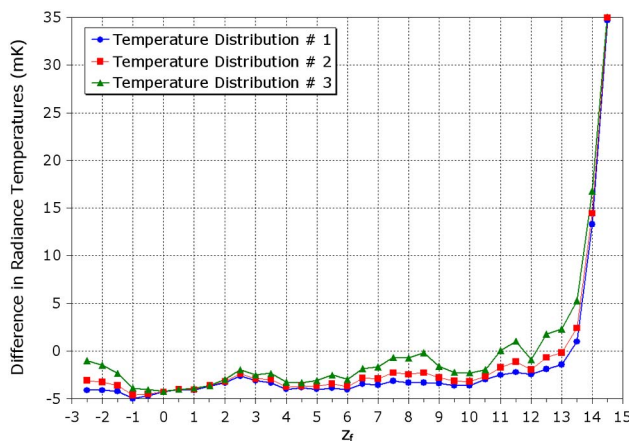


Fig. 11. (Color online) Deviation of radiance temperatures at $10.6 \mu\text{m}$ computed using the USD reflection model from those computed using 3C BRDF model. Difference in radiance temperatures is plotted as a function of the focal point position z_f of conical viewing conditions.

These examples show that the use of the USD reflection model instead of 3C BRDF model can, in some cases, lead to noticeable errors in calibration of various radiometric equipment including IR radiation thermometers due to oversimplified representation of the specular component.

All the numerical values in this section correspond to the example considered and do not allow deriving general recommendations; nonetheless, one can affirm that the maximal discrepancy between results computed using the 3C and the USD models is expected for cavities that have large angles between directions of observation and the normals to the directly viewable surface.

7. Conclusion

In this paper, we have presented the application of the 3C BRDF model to the MCRT calculation of spectral effective emissivities for nonisothermal blackbody cavities. An approach to extension of the monochromatic 3C model to the continuous spectral range was proposed. The MCRT algorithm for computing the spectral effective emissivities of the nonisothermal cavity was described and illustrated by the results of numerical experiments.

We have attempted to analyze some patterns in behavior of the results obtained; however, all the quantitative recommendations can only have task-specific character due to the large number of the affecting factors. To provide the highest precision in the effective emissivity calculations, every cavity has to be modeled individually, taking into account all geometric, optical, and temperature conditions. One thing is certain: the use of too simplified models of reflection (in particular, the USD model) for the effective emissivity calculations can result in non-negligible errors.

References

1. J. Hollandt, J. Seidel, R. Klein, G. Ulm, A. Migdall, and M. Ware, “Primary sources for use in radiometry,” in *Optical Radiometry*, A. C. Parr, R. U. Datla, and J. L. Gardner, eds. (Academic, 2005), pp. 213–290.
2. J. Hartmann, J. Hollandt, B. Khlevnoy, S. Morozova, S. Ogarev, and F. Sakuma, “Blackbody and other calibration sources,” in *Radiometric Temperature Measurements. I. Fundamentals*, Z. M. Zhang, B. K. Tsai, and G. Machin, eds. (Academic, 2010), pp. 241–295.
3. P. J. Mohr, B. N. Taylor, and D. B. Newell, “CODATA recommended values of the fundamental physical constants: 2010,” <http://physics.nist.gov/cuu/Constants/Preprints/Isa2010.pdf>.
4. S. N. Mekhontsev, A. V. Prokhorov, and L. N. Hanssen, “Experimental characterization of blackbody radiation sources,” in *Radiometric Temperature Measurements. II. Applications*, Z. M. Zhang, B. K. Tsai, and G. Machin, eds. (Academic, 2010), pp. 57–136.
5. R. E. Bedford, “Calculation of effective emissivities of cavity sources of thermal radiation,” in *Theory and Practice of Radiation Thermometry*, D. P. DeWitt and G. D. Nutter, eds. (Wiley, 1988), pp. 653–772.
6. A. V. Prokhorov, L. M. Hanssen, and S. N. Mekhontsev, “Calculation of the radiation characteristics of blackbody radiation sources,” in *Radiometric Temperature Measurements. I. Fundamentals*, Z. M. Zhang, B. K. Tsai, and G. Machin, eds. (Academic, 2010), pp. 181–240.

7. R. P. Heinisch, E. M. Sparrow, and N. Shamsundar, "Radiant emission from baffled conical cavities," *J. Opt. Soc. Am.* **63**, 152–158 (1973).
8. A. Ono, "Calculation of the directional emissivities of cavities by the Monte Carlo method," *J. Opt. Soc. Am.* **70**, 547–554 (1980).
9. V. I. Sapritsky and A. V. Prokhorov, "Spectral effective emissivities of nonisothermal cavities calculated by the Monte Carlo method," *Appl. Opt.* **34**, 5645–5652 (1995).
10. J. Ishii, M. Kobayashi, and F. Sakuma, "Effective emissivities of black-body cavities with grooved cylinders," *Metrologia* **35**, 175–180 (1998).
11. Y. Té, P. Jeseck, C. Camy-Peyret, S. Payan, S. Briau, and M. Fanjeaux, "High emissivity blackbody for radiometric calibration near ambient temperature," *Metrologia* **40**, 24–30 (2003).
12. M. J. Ballico, "Modelling of the effective emissivity of a graphite tube black body," *Metrologia* **32**, 259–265 (1995).
13. F. E. Nicodemus, J. C. Richmond, J. J. Hsia, I. W. Ginsberg, and T. Limperis, "Geometrical considerations and nomenclature for reflectance," NBS Monograph 160 (U. S. Department of Commerce, National Bureau of Standards, 1977).
14. A. Prokhorov, "Effective emissivities of isothermal blackbody cavities calculated by the Monte Carlo method using the three-component BRDF Model," *Appl. Opt.* **51**, 2322–2332 (2012).
15. H. J. Patrick, L. M. Hanssen, J. Zeng, and T. A. Germer, "BRDF measurements of graphite used in high-temperature fixed point blackbody radiators: a multi-angle study at 405 nm and 658 nm," *Metrologia* **49**, S81–S92 (2012).
16. M. Kurt and D. Edwards, "A survey of BRDF models for computer graphics," *Comput. Graph.* **43**, 4 (2009).
17. S. Liang, *Quantitative Remote Sensing of Land Surfaces* (Wiley, 2004).
18. D. Geisler-Moroder and A. Dür, "A new ward BRDF model with bounded albedo," *Comput. Graph. Forum* **29**, 1391–1398 (2010).
19. C. Schlick, "An inexpensive BRDF model for physically-based rendering," *Comput. Graph. Forum* **13**, 233–246 (1994).
20. M. Clerc, *Particle Swarm Optimization* (ISTE, 2006).
21. R. P. Brent, "An algorithm with guaranteed convergence for finding a zero of a function," *Comput. J. (Switzerland)* **14**, 422–425 (1971).
22. J. Berntsen, T. O. Espelid, and A. Genz, "An adaptive algorithm for the approximate calculation of multiple integrals," *ACM Trans. Math. Softw.* **17**, 437–451 (1991).
23. M. J. Persky, "Review of black surfaces for space-borne infrared systems," *Rev. Sci. Instrum.* **70**, 2193–2217 (1999).
24. L. M. Hanssen and A. V. Prokhorov, "Stochastic modeling of non-Lambertian surfaces for Monte Carlo computations in optical radiometry," *Proc. SPIE* **7427**, 742707 (2009).
25. Measurements were performed by Leonard M. Hanssen, Dr. (NIST, Gaithersburg, Maryland).
26. L. M. Hanssen and S. Kaplan, "Infrared diffuse reflectance instrumentation and standards at NIST," *Anal. Chim. Acta* **380**, 289–302 (1999).
27. J. Zeng and L. Hanssen, "An infrared laser-based reflectometer for low reflectance measurements of samples and cavity structures," *Proc. SPIE* **7065**, 70650F (2008).